IEEE Access
Multidisciplinary | Rapid Review | Open Access Journal

Received March 21, 2022, accepted March 26, 2022, date of publication April 5, 2022, date of current version April 12, 2022.

Digital Object Identifier 10.1109/ACCESS.2022.3165020

Translational Motion Compensation for ISAR Imaging Based on Range Joint Fast Orthogonal Matching Pursuit Algorithm

XU WEI, JUN YANG, MINGJIU LV, WENFENG CHEN, AND XIAOYAN MA
Air Force Early Warning Academy, Wuhan 430019, China

Corresponding author: Xu Wei (weixu_1003@163.com)

This work was supported in part by the National Natural Science Foundation of China under Grant 61671469, and in part the Dual Key Project.

ABSTRACT Accurate translational motion compensation (TMC) is the key procedure of inverse synthetic aperture radar (ISAR) imaging. Under the condition of sparse aperture, the correlation of adjacent pulses is severely destroyed, which brings a few challenges to TMC and imaging. Thus, this paper proposes a novel TMC method for ISAR imaging. In this technique, the signal model of joint phase adjustment and ISAR imaging is established first. Then, the process of TMC is designed. That is, after range alignment with improved global minimum entropy (IGME), the range joint fast orthogonal matching pursuit (RJFOMP) algorithm is applied to ISAR imaging, and the minimum entropy method (MEM) is adopted to estimate the phase error. Meanwhile, the joint optimization of phase adjustment and ISAR imaging is realized through the cyclic iteration. Extensive experiments based on both simulated and measured data demonstrate that the proposed TMC method is effective for two modes of motion errors, which are named as coherent mode (CM) and non-coherent mode (NCM), respectively. When RJFOMP is used for joint phase adjustment and ISAR imaging, it has excellent imaging performance under noisy and sparse conditions.

INDEX TERMS Inverse synthetic aperture radar (ISAR), translational motion compensation (TMC), improved global minimum entropy (IGME), range joint fast orthogonal matching pursuit (RJFOMP) algorithm, minimum entropy method (MEM).

I. INTRODUCTION

Benefiting from the ability of long-distance, all-time and all-weather detection for non-cooperative moving targets, inverse synthetic aperture radar (ISAR) plays an important role in military and civilian fields such as strategic early warning, space surveillance and target recognition [1]. With respect to ISAR imaging, the range resolution is related to the bandwidth of the radar transmitted signal, and the azimuth resolution depends on the coherent processing interval (CPI) and the angle of the target relative to the radar line of sight (RLOS) [2]. In the case of broad bandwidth and long CPI, the range-Doppler (RD) algorithm can be adopted to obtain two-dimensional high-resolution image of the target. However, in the actual imaging process, the radar time-sharing working mode and strong noise interference can cause limited or incomplete echo pulses, leading to sparse aperture, which may give rise to high side and grating lobes in RD imaging results, seriously affecting the imaging quality [3].

For the imaging problem under the condition of sparse aperture, traditional methods take some measures of extrapolation, interpolation and iterative convolution for missing data, such as Burg [4], RELAX [5] and CLEAN [6], which are usually prone to noise and model error, and have the problem of large computational complexity [7]. In recent years, compressive sensing (CS) theory [8] can realize high-precision reconstruction of undersampling data at a sampling frequency lower than Nyquist, which makes a revolutionary breakthrough in the field of signal processing. In view of the sparsity mechanism of targets in the imaging plane, CS theory can be introduced into ISAR imaging. By using the sparsity information of the target echo, the imaging problem under the condition of sparse aperture can be alleviated. At present, many feasible imaging algorithms have been proposed, such as

The associate editor coordinating the review of this manuscript and approving it for publication was Davide Comite.

orthogonal matching pursuit (OMP) algorithm [9], fast iterative shrinkage-thresholding algorithm (FISTA) [10], complex approximate message passing (CAMP) algorithm [11], alternating direction method of multipliers (ADMM) [12]–[15], adaptive gradient-based algorithm [16] and so on. All of them have achieved better imaging results than RD in different application scenarios. However, these imaging algorithms are usually based on effective translational motion compensation (TMC), which needs to be considered in advance before imaging.

In general, ISAR relies on the relative motion with the target to achieve its imaging results, and the relative motion can be decomposed into translational and rotational parts. The rotational motion produces the Doppler frequency required for imaging, which is the basis of target imaging. But the translational motion causes blurred and unfocused imaging results, which should be accurately compensated. The TMC is usually divided into two processing steps: range alignment and phase adjustment. The former realizes coarse compensation by eliminating the envelope offset of range profile, and the latter realizes fine compensation by correcting phase error. Typical range alignment methods are mainly sorted into two categories. One is based on the correlation of adjacent pulses, including maximum cross-correlation method [17] and cumulative cross-correlation method [18]. The other is global optimization methods, including global minimum entropy (GME) method [19], global maximum contrast (GMC) method [20] and Gram matrix method [21]. Classic phase adjustment methods can also be sorted into two categories. One is to track the phase of the main scattering centre, including Doppler centre tracking (DCT), phase gradient autofocus (PGA) algorithm [22] and eigenvector method [23]. The other is iterative processing based on image quality, which is carried out based on the criteria of minimum entropy [24] and maximum contrast [25] of imaging results. In addition, when the translational motion error is approximated as the polynomial model, range alignment and phase adjustment can be completed simultaneously by estimating the polynomial coefficients [2]. However, under the condition of sparse aperture, the correlation of adjacent pulses is severely destroyed, and range alignment methods based on global optimization are still effective, but the performance of traditional phase adjustment methods is degraded, which influences the effect of motion compensation. In order to reduce the influence of sparse aperture on phase adjustment, joint imaging and phase error correction technology in the autofocus problem of synthetic aperture radar (SAR) is proposed in [26] for the first time, which provides a solution to the problem of model error compensation in the sparse reconstruction. In [27], fast minimum entropy phase compensation (FMEPC) method is combined with smoothed l_0 norm (SL0) algorithm to realize the joint processing of phase adjustment and ISAR imaging, but it is sensitive to noise. In [28], an alternating direction iterative-shrinkage thresholding algorithm (ADI-STA) is proposed to realize the phase compensation and image autofocusing for randomized stepped frequency ISAR, but does not consider the influence of sparse aperture on imaging quality. In [29], [30], phase adjustment is integrated respectively into variational Bayesian inference (VBI) algorithm and ADMM for the iterative processing, which can realize both ISAR imaging and autofocusing, but the imaging performance decreases when the accuracy of range alignment is not enough.

With the aim of dealing with the above challenges effectively, a novel TMC method is proposed for ISAR imaging. Firstly, considering two modes of motion errors, the signal model of joint phase adjustment and ISAR imaging is established under the condition of sparse aperture. Then, the process of TMC method is given, which mainly includes two aspects. For one thing, an improved global minimum entropy (IGME) range alignment method is proposed to improve the accuracy of range alignment. For another, the joint optimization model of phase adjustment and ISAR imaging is constructed, the range joint fast orthogonal matching pursuit (RJFOMP) algorithm is applied to ISAR imaging to improve the imaging performance, and phase error estimation is realized based on the minimum entropy method (MEM) proposed in [29]. Finally, the effectiveness of the proposed TMC method for two modes of motion errors is verified by both simulated and measured data.

The rest of this paper is organized as follows. In Section II, the signal model of joint phase adjustment and ISAR imaging is established. In Section III, a novel TMC method is proposed in detail, including IGME range alignment method, the solution processes of RJFOMP and phase error estimation method. In Section IV, the experimental results based on both simulated and measured data are provided and analyzed, and a brief conclusion is summarized in Section IV.

II. SIGNAL MODEL

It is assumed that the radar transmits the linear frequency modulation (LFM) signal, which can be expressed as:

$$s\left(\hat{t}, t_m\right) = \text{rect}\left(\frac{\hat{t}}{T_\text{p}}\right) \exp\left[j2\pi\left(f_c t + \frac{1}{2}\gamma\hat{t}^2\right)\right] \tag{1}$$

where rect $(\cdot)$ denotes the unit rectangular function. T_p, f_c, γ, t, $\hat{t}$ and t_m denote the pulse width, carrier frequency, frequency modulation slope, full time, fast time and slow time, respectively. $t = \hat{t} + t_m$, $t_m = m \cdot \text{PRI}$, PRI is the pulse repetition interval, $m = 0, \cdots, M-1$, M is the number of pulses.

Supposing that the number of scattering points of the target is K_σ, the echo signal received by the radar is:

$$\begin{aligned} s_\text{r}\left(\hat{t}, t_m\right) = \sum_{i=1}^{K_\sigma} \sigma_i \text{rect}\left(\frac{\hat{t} - 2R_i\left(t_m\right)/c}{T_\text{p}}\right) \\ \cdot \exp\left\{j2\pi\left[f_c\left(t - \frac{2R_i\left(t_m\right)}{c}\right)\right.\right. \\ \left.\left. + \frac{1}{2}\gamma\left(\hat{t} - \frac{2R_i\left(t_m\right)}{c}\right)^2\right]\right\} \end{aligned} \tag{2}$$

where σ_i is the intensity of the i-th scattering point, and c is the light velocity. After Dechirp processing, compensations of the residual video phase (RVP) term and the envelope skew term [31], and range compression, the high-resolution range profile (HRRP) of the target can be expressed as:

$$S(f_r, t_m) = \sum_{i=1}^{K_\sigma} \sigma_i T_p \mathrm{sinc}\left[T_p\left(f_r + \frac{2\gamma}{c} R_\Delta^i(t_m)\right)\right] \cdot \exp\left(-j\frac{4\pi}{\lambda} R_\Delta^i(t_m)\right) \quad (3)$$

where f_r and $\lambda = c/f_c$ denote range frequency and the wavelength, respectively. $\mathrm{sinc}(u) = \sin(\pi u)/(\pi u)$, $R_\Delta^i(t_m) = R_i(t_m) - R_{\mathrm{ref}}$. Due to the non-cooperative motion of the target, the instantaneous distance $R_i(t_m)$ can be decomposed into translational and rotational parts. In general, the target rotates with small angle during short CPI. Let the reference distance meet: $R_{\mathrm{ref}} = R_0$, $R_\Delta^i(t_m)$ can be approximated as [1]:

$$R_\Delta^i(t_m) \approx R_T(t_m) + x_i \omega t_m + y_i \quad (4)$$

where (x_i, y_i) is the initial coordinate of the i-th scattering point of the target. $x_i = r_i \cos\theta_0$, $y_i = r_i \sin\theta_0$. r_i is the distance from the i-th scattering point to the coordinate origin, θ_0 is the initial rotation angle, and ω is the angular velocity. $R_T(t_m)$ is the instantaneous translation distance, which can produce motion errors during imaging. In practice, there are mainly two modes of motion errors in the echo signal received by the radar, namely coherent mode (CM) and non-coherent mode (NCM). The former is caused by the steady motion of the target, and the latter is caused by the severe vibration of the target or the range tracking error [18].

Ideally, when the range alignment is completed, the aligned HRRP can be expressed as:

$$S(f_r, t_m) = \sum_{i=1}^{K_\sigma} \sigma_i' \exp\left(-j\frac{4\pi}{\lambda} x_i \omega t_m\right) \exp\left(-j\frac{4\pi}{\lambda} R_T(t_m)\right) \quad (5)$$

where σ_i' is the intensity of the i-th scattering point after range alignment. The first phase term is the Doppler term required for imaging. The second phase term is the error term generated by the translational motion of the target, but in practice, the inaccurate range alignment and radar system noise will also introduce the phase errors related to slow time. For ease, they are uniformly recorded as $\exp(j\varphi(t_m))$, and the phase errors of all range cells in each HRRP are the same.

Under the condition of sparse aperture, (5) is written in the matrix form and the influence of additive complex Gaussian white noise is considered as well. Thus, the signal model of joint phase adjustment and ISAR imaging can be expressed as:

$$\mathbf{S} = \mathbf{EDFZ} + \mathbf{N} \quad (6)$$

where $\mathbf{S} \in \mathbb{C}^{L\times N}$, $\mathbf{Z} \in \mathbb{C}^{M\times N}$ and $\mathbf{N} \in \mathbb{C}^{L\times N}$ denote the HRRP matrix, ISAR imaging matrix to be reconstructed and noise matrix, respectively. N, M and L ($L \le M$) denote the number of range cells, azimuth cells and azimuth cells extracted from full aperture data, respectively. $\mathbf{E} \in \mathbb{C}^{L\times L}$ is a phase error matrix, $\mathbf{E} = \mathrm{diag}(\exp(\mathrm{j}\boldsymbol{\varphi}))$, with $\boldsymbol{\varphi} \in \mathbb{R}^{L\times 1}$ being a phase error vector, $\boldsymbol{\varphi} = [\varphi_1, \cdots, \varphi_L]^{\mathrm{T}}$, where $\mathrm{diag}(\mathbf{u})$ denotes a diagonal matrix with $\mathbf{u}$ as diagonal elements when $\mathbf{u}$ is a vector, and $\mathrm{diag}(\mathbf{u})$ denotes the column vector composed of diagonal elements of $\mathbf{u}$ when $\mathbf{u}$ is a matrix. $\mathbf{D} \in \mathbb{R}^{L\times M}$ is the azimuth undersampling matrix generated by randomly choosing L rows from $M-$ order unit matrix. $\mathbf{F} \in \mathbb{C}^{M\times M}$ is the azimuth sparse basis matrix, $\mathbf{F} = \exp\left(-j2\pi \mathbf{t}_s^{\mathrm{T}} \mathbf{f}_d\right)$, where $\mathbf{t}_s$ and $\mathbf{f}_d$ denote the slow time sequence and the Doppler sequence, respectively.

III. PROPOSED TMC METHOD

In the actual imaging process, the steady motion or severe vibration of non-cooperative targets and the range tracking error can produce motion errors, which may seriously affect the imaging quality. It is necessary to carry out accurate TMC before imaging. However, under the condition of sparse aperture, the performance of traditional phase adjustment methods is reduced and cannot meet the subsequent imaging requirements. Therefore, in this section, we first conduct range alignment, and then carry out the joint processing of phase adjustment and ISAR imaging to improve the imaging quality.

A. IGME RANGE ALIGNMENT METHOD

In order to realize range alignment of different motion error modes, GME range alignment method [19] takes the minimum average range profile entropy (ARPE) as the criterion for global iterative processing, does not need to assume the motion error model and traversal search operation, has good convergence and stability, and it belongs to the nonparametric method. On this basis, IGME range alignment method is proposed to improve the accuracy of range alignment and reduce the impact on the subsequent imaging quality through the interpolation processing.

Under the condition of sparse aperture, HRRP of (3) is further written as the discrete form $S(n, m)$, in which the unselected range profile sequence is set to zero, $n = 1, \cdots, N$ and $m = 1, \cdots, M$. Firstly, the interpolation processing in range direction is carried out, namely:

$$S'(n', m) = \mathrm{FFT}_c\left\{\mathrm{IFFT}_c\{S(n, m), N\}, N'\right\} \quad (7)$$

where $\mathrm{IFFT}_c\{\cdot, N\}$ and $\mathrm{FFT}_c\{\cdot, N'\}$ indicate that N-point inverse fast Fourier transform (IFFT) and N'-point fast Fourier transform (FFT) are performed by column, respectively. $n' = 1, \cdots, N'$, $N' = dN$. d is the interpolation multiple, and the accuracy of range alignment can be improved by d times.

Then, let $P(n', m) = |S'(n', m)|$, and supposing that the initial range shift compensated by the $m-$ th range profile is set to Δ_m^0, the initial average range profile (ARP) of $P(n', m)$

is calculated as:

$$P_{\text{ave}}^{0}\left(n'\right)=\sum_{m=1}^{M}P\left(n'+\Delta_{m}^{0},m\right) \tag{8}$$

According to the theoretical analysis results in [16], the iterative method of the optimal range shift is:

$$\begin{aligned}\Delta_{m}^{u}=&\Delta_{m}^{u-1}+\arg\max_{n'}\\&\times\left\{P\left(n'+\Delta_{m}^{u-1},m\right)*\ln\left(P_{\text{ave}}^{u-1}\left(-n'\right)\right)\right\}\end{aligned} \tag{9}$$

where u is the number of iterations, $u=1,2,\cdots$. "$*$" represents one-dimensional convolution operation, which can be efficiently implemented by the FFT and IFFT operations. When the ARPE difference between two adjacent iterations is less than σ_1, the final estimated range shift is Δ_m, and the output HRRP after range alignment is recorded as: $S_0'\left(n',m\right)=S'\left(n'+\Delta_m,m\right)$.

In order to maintain the same number of range cells as before the interpolation, the aligned HRRP is expressed as: $S_0\left(n,m\right)=S_0'\left(i,m\right)$, $i=\left(n-1\right)d+1$. If d is too large, the amount of computation increases, so set $d=\{1,\cdots,D_{\max}\}$. When the ARPE difference of the aligned HRRPs after two adjacent interpolations is less than σ_2, the final interpolation multiple D is output to achieve the purpose of balancing the accuracy and efficiency of range alignment.

B. JOINT PHASE ADJUSTMENT AND ISAR IMAGING

After the completion of range alignment, phase adjustment is usually required to obtain good imaging results, but residual errors may inevitably occur in the process of range alignment and phase adjustment due to inaccurate compensation, affecting the final imaging quality. Thus, phase adjustment and ISAR imaging are processed jointly after range alignment, and the focused imaging results are obtained through the cyclic iteration.

Because the targets satisfy the sparsity mechanism in the imaging plane, ISAR imaging can be transformed into a sparse reconstruction problem based on CS theory to improve the imaging resolution and alleviate the influence of sparse aperture. Considering the influence of phase error matrix $\mathbf{E}$, the loss function of joint phase adjustment and ISAR imaging is constructed as [26]:

$$J\left(\mathbf{Z},\mathbf{E}\right)=\frac{1}{2}\left\|\mathbf{S}-\mathbf{E}\boldsymbol{\Phi}\mathbf{Z}\right\|_{\text{F}}^{2}+\mu\left\|\mathbf{Z}\right\|_{1} \tag{10}$$

where $\boldsymbol{\Phi}\in\mathbb{C}^{L\times M}$ denotes the sensing matrix, $\boldsymbol{\Phi}=\mathbf{DF}$. μ is a regularization parameter, controlling the balance between image quality and sparsity. $\|\cdot\|_{\text{F}}$ and $\|\cdot\|_1$ denote the Frobenius norm and l_1 norm of the matrix, respectively. In the process of joint optimization of $\mathbf{Z}$ and $\mathbf{E}$, referring to the idea of coordinate descent, (10) is minimized through the cyclic iteration, that is, the following optimization problem is constructed as:

$$\begin{cases}\hat{\mathbf{Z}}^{(i+1)}=\arg\min\limits_{\mathbf{Z}}\ J\left(\mathbf{Z},\hat{\mathbf{E}}^{(i)}\right)\\ \hat{\mathbf{E}}^{(i+1)}=\arg\min\limits_{\mathbf{E}}\ J\left(\hat{\mathbf{Z}}^{(i+1)},\mathbf{E}\right)\end{cases} \tag{11}$$

where i is the number of iterations, $i=0,1,\cdots$. The first and second optimization problems are used to realize ISAR imaging and phase adjustment, respectively. In each iteration, CS algorithm is used for the sparse reconstruction, and then the phase error is updated based on the reconstruction result. Below, the theoretical analysis of these two optimization problems is mainly introduced in detail.

1) RJFOMP ALGORITHM

For the first optimization problem of (11), when the phase error matrix $\mathbf{E}$ is known and the superscript is ignored, it can be rewritten as:

$$\hat{\mathbf{Z}}=\arg\min_{\mathbf{Z}}\left\{\frac{1}{2}\left\|\mathbf{S}-\mathbf{A}\mathbf{Z}\right\|_{\text{F}}^{2}+\mu\left\|\mathbf{Z}\right\|_{1}\right\} \tag{12}$$

where $\mathbf{A}=\mathbf{E}\boldsymbol{\Phi}$, $\mathbf{A}\in\mathbb{C}^{L\times M}$. (12) is the standard form of basis pursuit denoising (BPDN) and LASSO, which is equivalent to the following equation:

$$\begin{aligned}\hat{\mathbf{Z}}=&\arg\min_{\mathbf{Z}}\left\{\left\|\mathbf{Z}\right\|_{1}\right\},\\&\text{s.t. }\left\|\mathbf{S}-\mathbf{A}\mathbf{Z}\right\|_{\text{F}}\leq\delta\end{aligned} \tag{13}$$

where δ is a constant related to noise energy, which can be estimated using the proposed method in [32].

Due to the non-cooperation and structural characteristics of the imaging target, the number of scattering points of $\mathbf{Z}$ in different range cells is usually different, and the support set after the sparse representation of $\mathbf{S}$ also changes over time. Therefore, the solution of $\mathbf{Z}$ is an arbitrary sparse structure reconstruction problem [1]. In order to solve (13) more effectively, RJFOMP algorithm is proposed based on OMP algorithm. It has three main advantages. Firstly, it has the advantages of simple structure, easy quantitative analysis and fast reconstruction speed like OMP algorithm. Secondly, compared with OMP algorithm, matrix vectorization and separate reconstruction of each range cell are avoided in ISAR imaging, and the joint reconstruction of different range cells is realized efficiently through the matrix operation. Thirdly, multi atom recognition and matrix recursive updating strategies are added to further improve the reconstruction speed of the algorithm. Next, the solution process of RJFOMP algorithm is given from three aspects: atomic recognition, projection update and residual update.

Let $\mathbf{A}=[\mathbf{a}_1,\cdots,\mathbf{a}_M]$, $\mathbf{I}=[\mathbf{i}_1,\cdots,\mathbf{i}_N]$, $\mathbf{I}\in\mathbb{R}^{N\times N}$ is the unit matrix. $\mathbf{a}_m\in\mathbb{C}^{L\times 1}$ and $\mathbf{i}_n\in\mathbb{C}^{N\times 1}$ denote the atom of the m-th and n-th column in $\mathbf{A}$ and $\mathbf{I}$, respectively, $\mathbf{a}_m=[a_{1m},\cdots,a_{Lm}]^{\text{T}}$, $\mathbf{i}_n=[i_{1n},\cdots,i_{Nn}]^{\text{T}}$. We define the matrix atom [33]: $\mathbf{C}_{mn}=\mathbf{a}_m\mathbf{i}_n^{\text{T}}$, $\mathbf{C}_{mn}\in\mathbb{C}^{L\times N}$, $\mathbf{S}$ can be expressed as

the linear combination of $\mathbf{C}_{mn}$:

$$\mathbf{S} = \sum_{m=1}^{M}\sum_{n=1}^{N} z_{mn}\mathbf{C}_{mn} \tag{14}$$

where z_{mn} is the element of $\mathbf{Z}$, and the estimate of z_{mn} can be expressed as: $\hat{z}_{mn} = \mathbf{a}_m^{\mathrm{H}}\mathbf{S}\mathbf{i}_n$.

In order to improve the reconstruction speed, supposing that v atoms (i.e. the atom selection step is v) are selected in each iteration in set $\Omega = \{(1,1), \cdots, (M,N)\}$, and the process of atom recognition in the k-th iteration is as follows:

$$\begin{aligned}\left(\hat{\mathbf{m}}_k, \hat{\mathbf{n}}_k\right) &= \arg\max_{\substack{v \\ (m,n)\in\Omega}} \left\{\left|\mathbf{a}_m^{\mathrm{H}}\mathbf{R}_{k-1}\mathbf{i}_n\right|\right\} \\ &= \arg\max_{\substack{v \\ (m,n)\in\Omega}} \left\{\left|\mathbf{A}^{\mathrm{H}}\mathbf{R}_{k-1}\right|\right\}\end{aligned} \tag{15}$$

where $\arg\max_v \{|\mathbf{u}|\}$ is to arrange $|\mathbf{u}|$ from largest to smallest and take out the position of the first v larger values. $\hat{\mathbf{m}}_k = \left\{\hat{m}_{(k-1)v+1}, \cdots, \hat{m}_{kv}\right\}$, $\hat{\mathbf{n}}_k = \left\{\hat{n}_{(k-1)v+1}, \cdots, \hat{n}_{kv}\right\}$. $\mathbf{R}_{k-1} \in \mathbb{C}^{L\times N}$ is the residual of $\mathbf{S}$ in the $(k-1)$ -th iteration, $\mathbf{R}_0 = \mathbf{S}$.

It is assumed that kv atoms have been selected in the k-th iteration, whose location set is denoted as $\Omega_k = \left\{\left(\hat{m}_1, \hat{n}_1\right), \cdots, \left(\hat{m}_{kv}, \hat{n}_{kv}\right)\right\}$, and the location set in $\mathbf{A}$ and $\mathbf{I}$ is denoted as $\Omega_k^1 = \left\{\hat{m}_1, \cdots, \hat{m}_{kv}\right\}$ and $\Omega_k^2 = \left\{\hat{n}_1, \cdots, \hat{n}_{kv}\right\}$, respectively. Let $\mathbf{A}_{\Omega_k^1} = \left[\mathbf{a}_{\hat{m}_1}, \cdots, \mathbf{a}_{\hat{m}_{kv}}\right]$, $\mathbf{I}_{\Omega_k^2} = \left[\mathbf{i}_{\hat{n}_1}, \cdots, \mathbf{i}_{\hat{n}_{kv}}\right]$, $\hat{\mathbf{z}}_k = \left[z_{\hat{m}_1\hat{n}_1}, \cdots, z_{\hat{m}_{kv}\hat{n}_{kv}}\right]^{\mathrm{T}}$, the estimated value $\hat{\mathbf{S}}_k$ of $\mathbf{S}$ composed of kv atoms is expressed as:

$$\hat{\mathbf{S}}_k = \sum_{p=1}^{kv} z_{\hat{m}_p\hat{n}_p}\mathbf{C}_{\hat{m}_p\hat{n}_p} = \mathbf{A}_{\Omega_k^1}\mathrm{diag}\left(\hat{\mathbf{z}}_k\right)\mathbf{I}_{\Omega_k^2}^{\mathrm{T}} \tag{16}$$

To get the optimal $\hat{\mathbf{z}}_k$, the minimization problem of the residual of $\mathbf{S}$ is constructed as [33]:

$$\hat{\mathbf{z}}_k = \arg\min_{\mathbf{z}_k}\left\{\|\mathbf{R}_k\|_{\mathrm{F}}\right\} \Leftrightarrow \hat{\mathbf{z}}_k = \arg\min_{\mathbf{z}_k}\left\{\mathrm{tr}\left(\mathbf{R}_k^{\mathrm{H}}\mathbf{R}_k\right)\right\} \tag{17}$$

where $\mathbf{R}_k = \mathbf{S} - \hat{\mathbf{S}}_k$, and $\mathrm{tr}(\cdot)$ denotes the trace of the matrix. $\mathrm{tr}\left(\mathbf{R}_k^{\mathrm{H}}\mathbf{R}_k\right)$ is:

$$\begin{aligned}&\mathrm{tr}\left(\mathbf{R}_k^{\mathrm{H}}\mathbf{R}_k\right) \\ &= \mathrm{tr}\left(\mathbf{S} - \sum_{p=1}^{kv} z_{\hat{m}_p\hat{n}_p}\mathbf{C}_{\hat{m}_p\hat{n}_p}\right)^{\mathrm{H}}\left(\mathbf{S} - \sum_{q=1}^{kv} z_{\hat{m}_q\hat{n}_q}\mathbf{C}_{\hat{m}_q\hat{n}_q}\right) \\ &= \mathrm{tr}\left(\mathbf{S}^{\mathrm{H}}\mathbf{S}\right) + \sum_{p=1}^{kv}\sum_{q=1}^{kv} z_{\hat{m}_p\hat{n}_p}^{*} z_{\hat{m}_q\hat{n}_q}\mathbf{W}_k^{pq} - \sum_{p=1}^{kv} z_{\hat{m}_p\hat{n}_p}^{*}\tilde{\mathbf{F}}_k^{p} \\ &\quad - \sum_{q=1}^{kv} z_{\hat{m}_q\hat{n}_q}\left(\tilde{\mathbf{F}}_k^{q}\right)^{\mathrm{H}} \\ &= \|\mathbf{S}\|_{\mathrm{F}}^2 + \hat{\mathbf{z}}_k^{\mathrm{H}}\mathbf{W}_k\hat{\mathbf{z}}_k - \hat{\mathbf{z}}_k^{\mathrm{H}}\tilde{\mathbf{F}}_k - \tilde{\mathbf{F}}_k^{\mathrm{H}}\hat{\mathbf{z}}_k\end{aligned} \tag{18}$$

where $\mathbf{W}_k^{pq}$ and $\tilde{\mathbf{F}}_k^{p}$ denote the element of $\mathbf{W}_k \in \mathbb{C}^{kv\times kv}$ and $\tilde{\mathbf{F}}_k \in \mathbb{C}^{kv\times 1}$, respectively. $\mathbf{W}_k^{pq}$ and $\tilde{\mathbf{F}}_k^{p}$ are:

$$\begin{cases}\mathbf{W}_k^{pq} = \mathrm{tr}\left(\mathbf{C}_{\hat{m}_p\hat{n}_p}^{\mathrm{H}}\mathbf{C}_{\hat{m}_q\hat{n}_q}\right) = \mathrm{tr}\left(\mathbf{i}_{\hat{n}_p}\mathbf{a}_{\hat{m}_p}^{\mathrm{H}}\mathbf{a}_{\hat{m}_q}\mathbf{i}_{\hat{n}_q}^{\mathrm{T}}\right) \\ \qquad\quad = \mathbf{a}_{\hat{m}_p}^{\mathrm{H}}\mathbf{a}_{\hat{m}_q}\mathbf{i}_{\hat{n}_p}^{\mathrm{T}}\mathbf{i}_{\hat{n}_q} \\ \tilde{\mathbf{F}}_k^{p} = \mathrm{tr}\left(\mathbf{C}_{\hat{m}_p\hat{n}_p}^{\mathrm{H}}\mathbf{S}\right) = \mathrm{tr}\left(\mathbf{i}_{\hat{n}_p}\mathbf{a}_{\hat{m}_p}^{\mathrm{H}}\mathbf{S}\right) = \mathbf{a}_{\hat{m}_p}^{\mathrm{H}}\mathbf{S}\mathbf{i}_{\hat{n}_p}\end{cases} \tag{19}$$

And $\mathbf{W}_k$ and $\tilde{\mathbf{F}}_k$ can be expressed as:

$$\begin{cases}\mathbf{W}_k = \left(\mathbf{A}_{\Omega_k^1}^{\mathrm{H}}\mathbf{A}_{\Omega_k^1}\right)\odot\left(\mathbf{I}_{\Omega_k^2}^{\mathrm{T}}\mathbf{I}_{\Omega_k^2}\right) \\ \tilde{\mathbf{F}}_k = \mathrm{diag}\left(\mathbf{A}_{\Omega_k^1}^{\mathrm{H}}\mathbf{S}\mathbf{I}_{\Omega_k^2}\right)\end{cases} \tag{20}$$

where "$\odot$" denotes the Hadamard product. When $\mathrm{tr}\left(\mathbf{R}_k^{\mathrm{H}}\mathbf{R}_k\right)$ is the minimum, we have:

$$\mathrm{d}\left[\mathrm{tr}\left(\mathbf{R}_k^{\mathrm{H}}\mathbf{R}_k\right)\right]\Big/\mathrm{d}\left(\hat{\mathbf{z}}_k\right) = 2\mathbf{W}_k\hat{\mathbf{z}}_k - 2\tilde{\mathbf{F}}_k = \mathbf{0} \tag{21}$$

Then, the process of projection update in the k-th iteration is as follows:

$$\hat{\mathbf{z}}_k = \mathbf{W}_k^{-1}\tilde{\mathbf{F}}_k \tag{22}$$

With the increase of the number of iterations, the dimension of $\mathbf{W}_k$ is also increasing, leading to the increase in the amount of computation of the inverse operation. Thus, a matrix recursive updating strategy is proposed. From (19), $\mathbf{W}_k$ and $\mathbf{W}_{k-1}$ have the following relationship:

$$\mathbf{W}_k = \begin{bmatrix}\mathbf{W}_{k-1} & \mathbf{g}_k \\ \mathbf{g}_k^{\mathrm{H}} & \boldsymbol{\kappa}_k\end{bmatrix} \tag{23}$$

where $\mathbf{g}_k \in \mathbb{C}^{(k-1)v\times v}$ and $\boldsymbol{\kappa}_k \in \mathbb{C}^{v\times v}$ can be constructed according to (19), respectively.

Adopting the inverse lemma of block matrix [34], the inverse matrix of $\mathbf{W}_k$ can be simplified to:

$$\begin{aligned}\mathbf{W}_k^{-1} &= \begin{bmatrix}\mathbf{W}_{k-1} & \mathbf{g}_k \\ \mathbf{g}_k^{\mathrm{H}} & \boldsymbol{\kappa}_k\end{bmatrix}^{-1} \\ &= \begin{bmatrix}\mathbf{W}_{k-1}^{-1} + \mathbf{d}_k\boldsymbol{\alpha}_k\mathbf{d}_k^{\mathrm{H}} & -\mathbf{d}_k\boldsymbol{\alpha}_k \\ -\boldsymbol{\alpha}_k\mathbf{d}_k^{\mathrm{H}} & \boldsymbol{\alpha}_k\end{bmatrix}\end{aligned} \tag{24}$$

where $\mathbf{d}_k = \mathbf{W}_{k-1}^{-1}\mathbf{g}_k$, and $\boldsymbol{\alpha}_k = \left(\boldsymbol{\kappa}_k - \mathbf{g}_k^{\mathrm{H}}\mathbf{d}_k\right)^{-1}$.

Ultimately, Combined with (16), the process of residual update in the k-th iteration is as follows:

$$\mathbf{R}_k = \mathbf{S} - \mathbf{A}_{\Omega_k^1}\mathrm{diag}\left(\hat{\mathbf{z}}_k\right)\mathbf{I}_{\Omega_k^2}^{\mathrm{T}} \tag{25}$$

To sum up, according to the iteration of (15), (22) and (25), we can obtain the location sets Ω^1 and Ω^2, and the estimated value $\hat{\mathbf{z}}$ of selected atoms, then the ISAR imaging result is expressed as: $\mathbf{Z}\left(\Omega^1, \Omega^2\right) = \hat{\mathbf{z}}$, where $\mathbf{Z}$ is initialized to the zero matrix.

2) PHASE ERROR ESTIMATION BASED ON MEM

For the second optimization problem of (11), in order to realize phase adjustment, MEM is used to estimate the phase error matrix $\mathbf{E}$. According to the ISAR imaging result $\mathbf{Z}$, the entropy of which is defined as [29]:

$$E_{\mathbf{Z}} = -\sum_{m=1}^{M}\sum_{n=1}^{N} |z_{mn}|^2 \ln |z_{mn}|^2 \tag{26}$$

where z_{mn} is the element of the m-th row and n-th column in $\mathbf{Z}$.

With the minimum of $E_{\mathbf{Z}}$ as the objective function, $\mathbf{E}$ can be obtained by solving the optimization problem $\hat{\mathbf{E}} = \arg\min_{\mathbf{E}} \{E_{\mathbf{Z}}\}$. The first partial derivative of $E_{\mathbf{Z}}$ with respect to phase error φ_l is calculated as:

$$\frac{\partial E_{\mathbf{Z}}}{\partial \varphi_l} = -\sum_{m=1}^{M}\sum_{n=1}^{N} \left(1 + \ln |z_{mn}|^2\right) \frac{\partial |z_{mn}|^2}{\partial \varphi_l} \tag{27}$$

where $\partial |z_{mn}|^2 \big/ \partial \varphi_l = 2\mathrm{Re}\left\{z_{mn}^* \cdot \partial z_{mn} \big/ \partial \varphi_l\right\}$, $\mathrm{Re}\{\cdot\}$ represents the real part. Convert $\mathbf{Z} = \mathbf{\Phi}^{\mathrm{H}}\mathbf{E}^{\mathrm{H}}\mathbf{S}$ into the matrix element operation to obtain $z_{mn} = \sum_{l=1}^{L} \phi_{lm}^* s_{ln} \exp(-j\varphi_l)$, in which ϕ_{lm} is the element of the l-th row and m-th column in $\mathbf{\Phi}$, s_{ln} is the element of the l-th row and n-th column in $\mathbf{S}$. Then, the first partial derivative of z_{mn} with respect to phase error φ_l is $\partial z_{mn} \big/ \partial \varphi_l = -j\phi_{lm}^* s_{ln} \exp(-j\varphi_l)$, and substituting it into (27), we can obtain:

$$\frac{\partial E_{\mathbf{Z}}}{\partial \varphi_l} = -2\mathrm{Im} \times \left\{\exp(-\mathrm{j}\varphi_l) \sum_{m=1}^{M}\sum_{n=1}^{N} \left(1 + \ln |z_{mn}|^2\right) z_{mn}^* \phi_{lm}^* s_{ln}\right\} \tag{28}$$

where $\mathrm{Im}\{\cdot\}$ represents the imaginary part. Let $\partial E_{\mathbf{Z}} \big/ \partial \varphi_l = 0$, the phase error φ_l is estimated as:

$$\hat{\varphi}_l = \mathrm{angle}\left\{\sum_{m=1}^{M}\sum_{n=1}^{N} \left(1 + \ln |z_{mn}|^2\right) z_{mn}^* \phi_{lm}^* s_{ln}\right\} \tag{29}$$

where $\mathrm{angle}\{\cdot\}$ represents the angle. The phase error vector $\boldsymbol{\varphi}$ is estimated as:

$$\hat{\boldsymbol{\varphi}} = \mathrm{angle}\left\{\mathrm{diag}\left(\mathbf{S}\left((1 + \ln(|\mathbf{Z}| \odot |\mathbf{Z}|)) \odot \mathbf{Z}\right)^{\mathrm{H}} \mathbf{\Phi}^{\mathrm{H}}\right)\right\} \tag{30}$$

Thus, the estimated value of $\mathbf{E}$ is $\hat{\mathbf{E}} = \mathrm{diag}\left(\exp\left(\mathrm{j}\hat{\varphi}\right)\right)$.

3) FLOWCHART AND COMPUTATIONAL DETAILS

The flowchart of the proposed TMC method is shown in Fig. 1. In Fig. 1, the raw echo signal received by the radar is preprocessed to obtain HRRP matrix $\mathbf{S}$ first. Then, the range alignment is realized based on IGME, and the joint processing of phase adjustment and ISAR imaging is completed through the cyclic iteration.

For parameter initialization, in IGME, the small value σ_1 and σ_2 are set to 10^{-6} and 10^{-4}, respectively. The maximum interpolation multiple $D_{\max}$ is set to 10. In RJFOMP, the preset sparsity $K_{\max}$ can be approximately estimated by the atomic matching test [35]. The atom selection step v meets [36]: $v \le \sqrt{LN}$, and we roughly set $v \approx 0.5\sqrt{LN}$ for the balance of reconstruction speed and accuracy. The stop threshold ε [37] is set to $\varepsilon = c\|\mathbf{S}\|_{\mathrm{F}}$, $c \in [0, 0.5]$, and c is simply set to 0.5 in this paper.

In order to accelerate the convergence speed of the cyclic iteration, the initial value of the ISAR imaging result is set to $\hat{\mathbf{Z}}^{(0)} = \mathbf{\Phi}^{\mathrm{H}}\hat{\mathbf{E}}^{(0)\mathrm{H}}\mathbf{S}$. The initial value of the phase error matrix is set to $\hat{\mathbf{E}}^{(0)} = \mathrm{diag}\left(\exp\left(\mathrm{j}\boldsymbol{\varphi}^{(0)}\right)\right)$, in which the relationship between adjacent phase errors is $\varphi_{p+1}^{(0)} = \varphi_p^{(0)} \cdot ss/|ss|$, $ss = \sum_{n=1}^{N} s_{pn}^* s_{(p+1)n}$, $\varphi_1^{(0)} = 1$ and $p = 1, \cdots, L-1$. In addition, if the relative error meets: $re = \left\|\hat{\mathbf{Z}}^{(i+1)} - \hat{\mathbf{Z}}^{(i)}\right\|_{\mathrm{F}}^2 \Big/ \left\|\hat{\mathbf{Z}}^{(i)}\right\|_{\mathrm{F}}^2 < err$ or i reaches the preset maximum number of iterations $I_{\max}$, the iteration is ended in advance and the ISAR imaging result are output. In general, when err is set to 0.01 or 0.001 and $I_{\max}$ is set to 100, a good imaging result can be obtained, and the computational complexity of the cyclic iteration is relatively small.

In the end, we further analyze the computational complexity of the proposed TMC method, which consists of IGME, RJFOMP and MEM. IGME adds the interpolation processing based on GME. The main computational burden of GME comes from a few FFT and IFFT operations. Assuming that the number of iterations of the optimal range shift in GME is N_1, the computational complexity of the d-th interpolation processing of IGME is approximately $O\left(dNN_1M\log_2(dN)\right)$. Let final interpolation multiple be D, the computational complexity of IGME is approximately $O\left(D^2NN_1M\log_2(DN)\right)$. If the number of iterations of RJFOMP is N_2, its main computational burden is determined by three aspects: atomic recognition, projection update and residual update, and the computational complexity of three aspects is approximately $O(N_2LMN)$, $O\left(N_2^3v^3 + N_2^3Nv^2 + N_2^2NLv\right)$ and $O\left(N_2^3Lv^2 + N_2^2NLv\right)$, respectively. For MEM, it mainly involves matrix multiplication operations, and its computational complexity is approximately $O\left(LMN + L^2M\right)$. Therefore, it is assumed that the number of iterations of phase adjustment and ISAR imaging is N_3, the total computational complexity of the proposed TMC method is approximately

$$O\Big(D^2NN_1M\log_2(DN) + N_3\left(L^2M + N_2LMN + N_2^3v^3 + N_2^3Nv^2 + N_2^3Lv^2 + N_2^2NLv\right)\Big).$$

IV. EXPERIMENTS AND ANALYSIS

In this section, in order to verify the effectiveness of the proposed TMC method, the influence of range alignment method (RAM) on imaging performance is discussed first. Then, the characteristics of the joint processing of phase adjustment and ISAR imaging are analyzed. In the end, the

TABLE 1. Main radar parameters of four groups of data.

Parameters	data1	data2	data3	data4
frequency	10GHz	10GHz	S-band	5.52GHz
bandwidth	600MHz	600MHz	100MHz	400MHz
PRF	200Hz	200Hz	410Hz	400Hz
pulse width	150μs	150μs	200μs	25.6μs
range cell	256	256	600	256
azimuth cell	256	256	256	256
motion error	CM	NCM	CM	NCM

imaging performance of different CS algorithms for phase adjustment and ISAR imaging is compared.

A. PARAMETER SETTING AND EVALUATION INDEXES

Combined with two modes of motion errors existing in the actual imaging, four groups of data are selected for subsequent experiments, in which data1 and data2 are simulated data, and data3 and data4 are measured data. The main radar parameter settings are shown in Table 1. Here, it should be noted that data1 and data2 are artificially generated target echo data. The instantaneous translational distance of data1 is set to the polynomial form to simulate the motion error of CM, namely: $R_{\mathrm{T}}(t_m) = v_r t_m + (1/2)\, a_r t_m^2$, in which the radial translational velocity v_r and acceleration a_r of the target are set as 150m/s and 1.35m/s^2, respectively. The instantaneous translational distance of data2 is set to the random form to simulate the motion error of NCM, namely: $R_{\mathrm{T}}(t_m) = \mathrm{unifrnd}(-10, 10)$, in which $\mathrm{unifrnd}(a, b)$ denotes generating random numbers in the interval (a, b). Data3 and data4 represent the measured data with motion errors of CM and NCM, respectively. In addition to the known radar parameters, other motion parameters of the target are unknown. But these parameters do not affect the effectiveness of the proposed method, because IGME is the nonparametric range alignment method, and the joint processing of phase adjustment and ISAR imaging does not need to clarify the motion parameters of the target as well.

In addition, the performance of range alignment is measured by the ARPE. The smaller the ARPE is, the better the performance is. Assuming that the unselected range profile sequence is set to zeros, and the HRRP matrix after the operation of modulus is recorded as $\tilde{\mathbf{S}} = (\tilde{s}_{nm})_{N\times M}$, $\mathbf{S} = \left|\mathbf{S}^{\mathrm{T}}\mathbf{D}\right|$, then ARPE is defined as [19]:

$$\mathrm{ARPE} = -\sum_{n=1}^{N} \frac{\mathrm{ave}_n}{\mathrm{sum}_{\tilde{\mathbf{S}}}} \ln \frac{\mathrm{ave}_n}{\mathrm{sum}_{\tilde{\mathbf{S}}}} \tag{31}$$

where $\mathrm{ave}_n = \sum_{m=1}^{M} \tilde{s}_{nm}$, and $\mathrm{sum}_{\tilde{\mathbf{S}}} = \sum_{n=1}^{N}\sum_{m=1}^{M} \tilde{s}_{nm}$.

The imaging performance is evaluated by image entropy (IE) [38], image contrast (IC) [3] and running time (Time), in which the running time is obtained by a platform of $IntelCorei5-8250U@1.60GHz$. The smaller the IE is, the larger the IC is, and the better the imaging quality is. The smaller the Time is, and the faster the imaging speed is. In our all experiments, "Time" represents the time of the joint processing of phase adjustment and ISAR imaging, and does not include the time of range alignment.

B. PERFORMANCE ANALYSIS OF RANGE ALIGNMENT METHOD

Based on four groups of data, the effect of GME and IGME on imaging performance is analyzed. First of all, we give the definitions of signal-to-noise ratio (SNR) and azimuth sparsity rate (ASR) in this paper. SNR is defined as the ratio of echo signal energy after pulse compression to noise energy. ASR is defined as the ratio of the number of pulses taken out to the total number of pulses. The simulation conditions of four groups of data are given as follows. Data1 and data2 are discussed when SNR = 5dB and ASR = 0.5. Data3 and data4

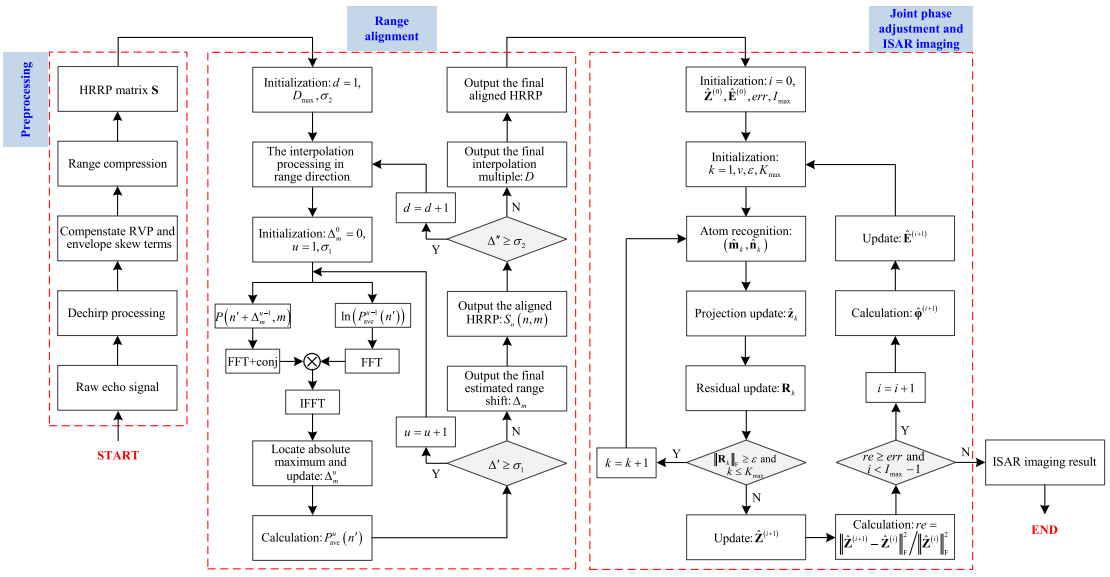

FIGURE 1. Flowchart of the proposed TMC method.

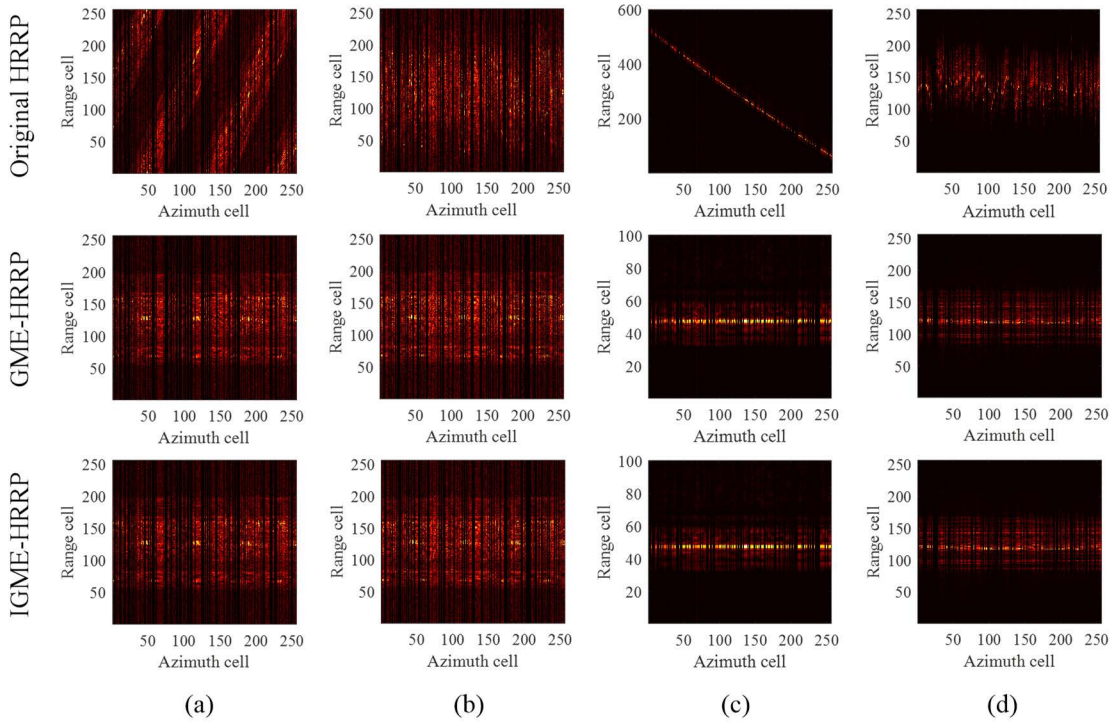

FIGURE 2. HRRPs before and after range alignment. (a) data1; (b) data2; (c) data3; (d) data4.

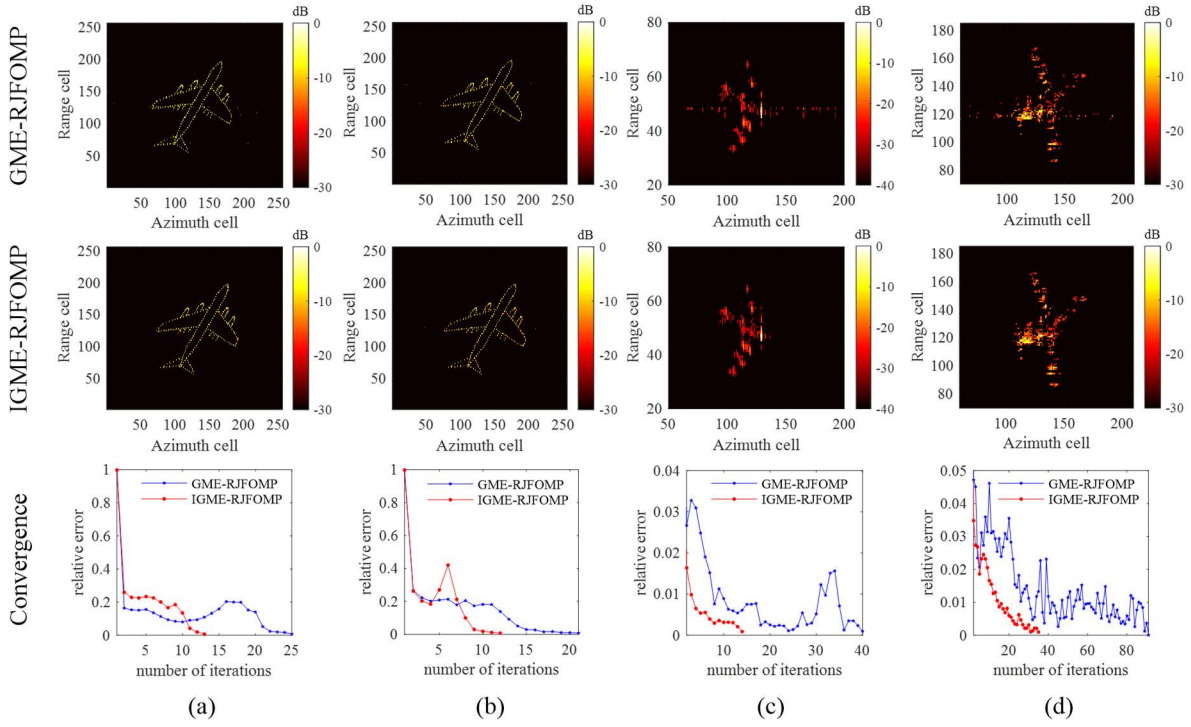

FIGURE 3. Imaging results and convergence. (a) data1; (b) data2; (c) data3; (d) data4.

are discussed when there is no noise and ASR = 0.5. Then, HRRPs before and after GME and IGME range alignment are shown in Fig. 2. Combined with RJFOMP algorithm, imaging results after the joint processing of phase adjustment and ISAR imaging and the convergence of the cyclic iteration are shown in Fig. 3. Lastly, ARPE of HRRPs after range alignment in Fig. 2 and IE, IC and Time of imaging results in Fig. 3 are calculated in Table 2.

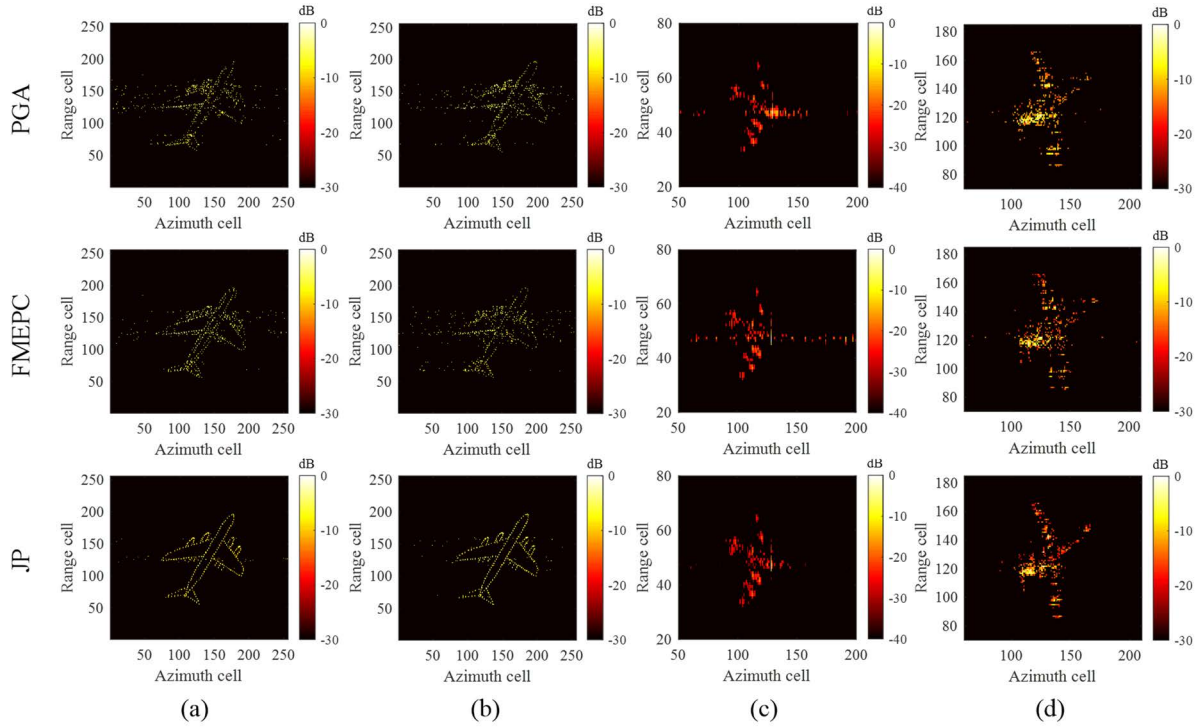

FIGURE 4. Imaging results of joint processing and separate processing. (a) data1; (b) data2; (c) data3; (d) data4.

TABLE 2. Index values in Figs. 2 and 3.

data	RAMs	ARPE	IE	IC	Time(s)
1	GME	5.4246	6.3619	10.7911	5.5057
	IGME	5.4234	6.3598	10.8134	2.8408
2	GME	5.4268	6.3630	10.7845	4.4694
	IGME	5.4258	6.3579	10.8437	2.6382
3	GME	3.7962	4.8783	20.9713	2.3933
	IGME	3.7848	4.8151	21.9450	0.8970
4	GME	4.8472	5.8679	14.7360	14.9929
	IGME	4.8396	5.8471	15.0397	5.8099

It can be seen from Figs. 2 and 3 that the range alignment accuracy of IGME is higher than that of GME. The imaging results of IGME combined with RJFOMP algorithm are better than GME, and the convergence times of the cyclic iteration are less, indicating that the accuracy of range alignment can affect the imaging performance of subsequent joint processing of phase adjustment and ISAR imaging. This conclusion can also be verified in Table 2. IGME range alignment method has smaller ARPE, and imaging results also have smaller IE and Time, and larger IC. Meanwhile, according to the imaging results and convergence, IGME range alignment method is effective for two modes of motion errors, and the sensitivity of simulated data to range alignment accuracy is weak, while the measured data has higher requirements for the accuracy of range alignment.

C. CHARACTERISTIC ANALYSIS OF THE JOINT PROCESSING OF PHASE ADJUSTMENT AND ISAR IMAGING

In order to analyze the characteristics of the joint processing of phase adjustment and ISAR imaging, traditional separate processing algorithms are compared with the joint processing (JP) algorithm in this paper by combining four groups of data. Firstly, set the simulation conditions of data1 and data2 as SNR = 5dB and ASR = 0.3, and the simulation conditions of data3 and data4 as no noise and ASR = 0.3. Then, after the IGME range alignment, two separate processing algorithms (that is, PGA and FMEPC are used for phase adjustment respectively, and RJFOMP is used for imaging) are selected and compared with the joint processing algorithm, the imaging results of three algorithms are shown in Fig. 4. The IE, IC and Time of imaging results in Fig. 4 are calculated in Table 3.

TABLE 3. IE, IC and time of imaging results in Fig. 4.

data	Algorithms	IE	IC	Time(s)
1	PGA	6.3671	10.7327	0.3625
	FMEPC	6.3658	10.7483	1.9770
	JP	6.3539	10.8769	3.7989
2	PGA	6.3696	10.7047	0.3879
	FMEPC	6.3665	10.7409	2.0078
	JP	6.3597	10.8082	7.4624
3	PGA	4.9556	18.4343	0.0596
	FMEPC	4.9899	18.0144	0.8608
	JP	4.8311	22.0093	0.4570
4	PGA	5.8861	14.3273	0.2153
	FMEPC	5.8632	14.7128	6.4222
	JP	5.8430	15.0673	11.0116

In Fig. 4, we can know that the two separate processing algorithms degrade the imaging quality due to inaccurate phase adjustment, while joint phase adjustment and ISAR imaging has the best imaging quality for four groups of data, and also has the smallest IE and the largest IC in Table 3.

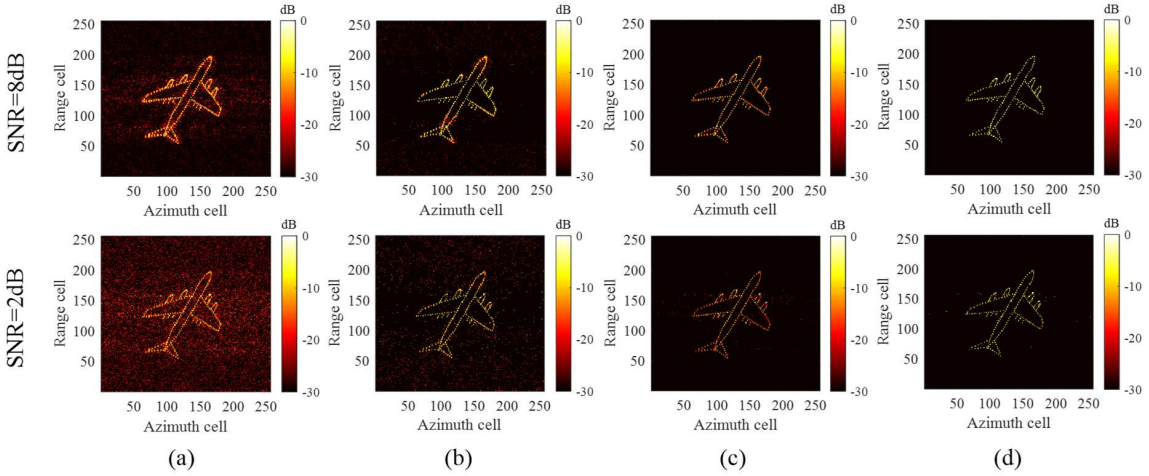

FIGURE 5. Imaging results of different algorithms under different SNRs for data1. (a) SL0; (b) OMP; (c) FISTA; (d) RJFOMP.

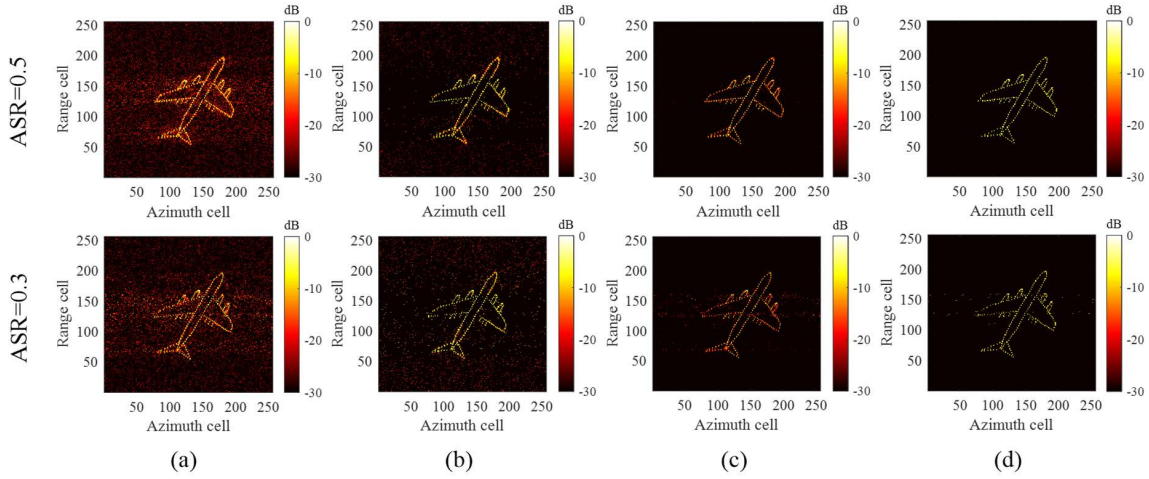

FIGURE 6. Imaging results of different algorithms under different ASRs for data1. (a) SL0; (b) OMP; (c) FISTA; (d) RJFOMP.

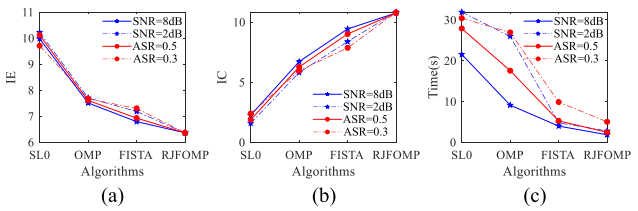

FIGURE 7. IE, IC and time of imaging results in Figs. 5 and 6. (a) IE; (b) IC; (c) Time.

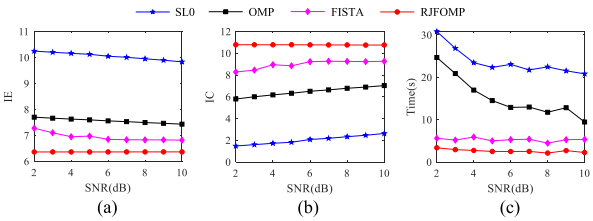

FIGURE 8. Monte-Carlo experimental results of SNR for data1. (a) IE; (b) IC; (c) Time.

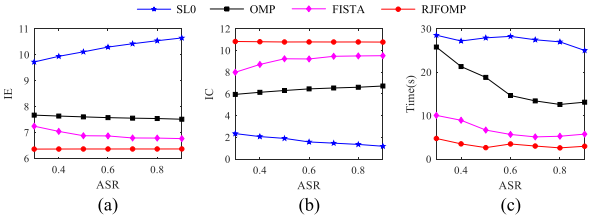

FIGURE 9. Monte-Carlo experimental results of ASR for data1. (a) IE; (b) IC; (c) Time.

However, the imaging time of the joint processing is the longest, indicating that the joint processing improves the imaging quality at the time cost of the cyclic iteration, and is suitable for imaging scenes with low time requirements.

D. IMAGING PERFORMANCE COMPARISON OF DIFFERENT ALGORITHMS

In the process of joint phase adjustment and ISAR imaging, different imaging algorithms may affect the results of the joint processing. Therefore, under different SNRs and ASRs, combined with four groups of data, the imaging performance of RJFOMP proposed in this paper is compared with SL0 [24], OMP [9] and FISTA [10] algorithms.

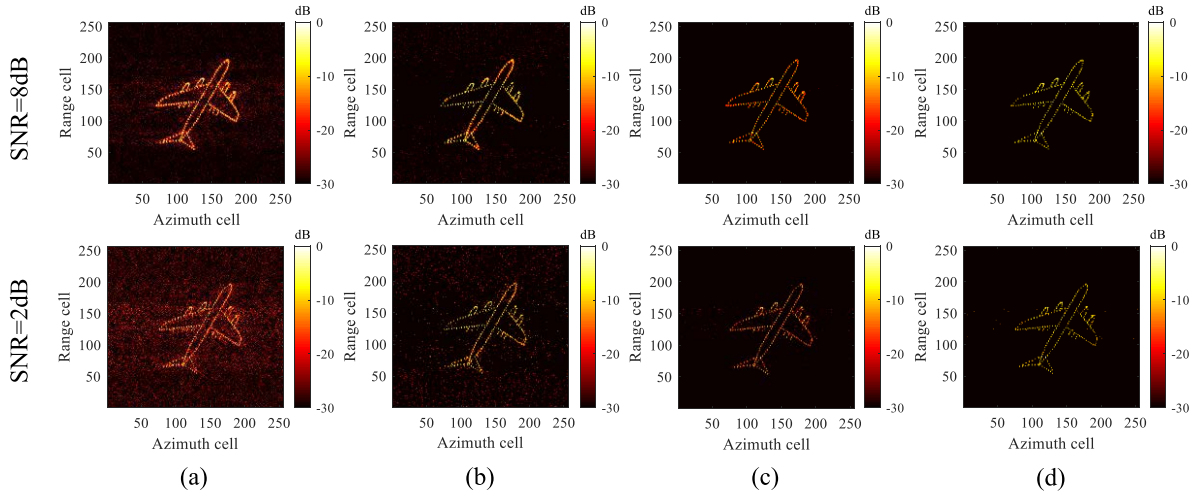

FIGURE 10. Imaging results of different algorithms under different SNRs for data2. (a) SL0; (b) OMP; (c) FISTA; (d) RJFOMP.

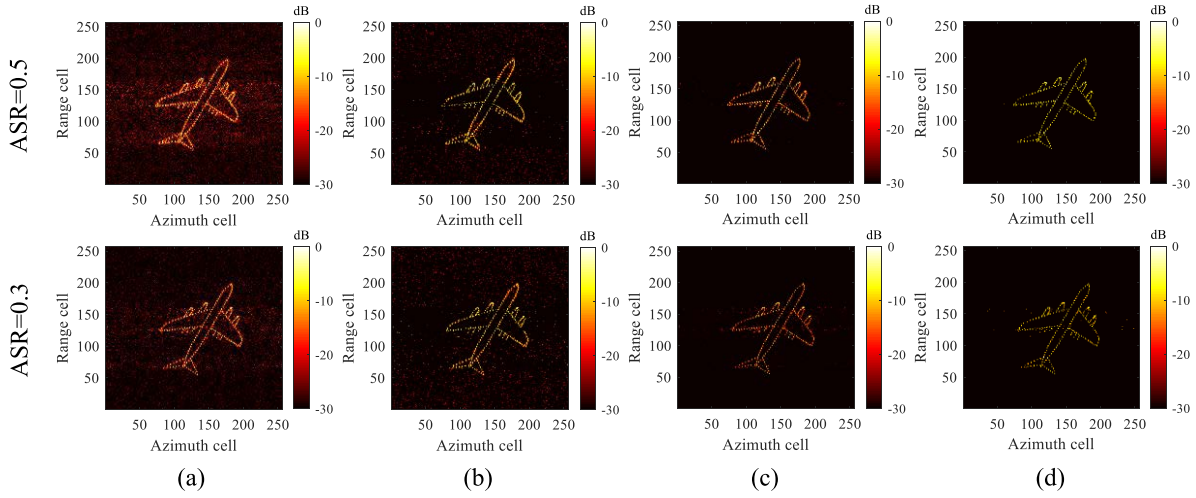

FIGURE 11. Imaging results of different algorithms under different ASRs for data2. (a) SL0; (b) OMP; (c) FISTA; (d) RJFOMP.

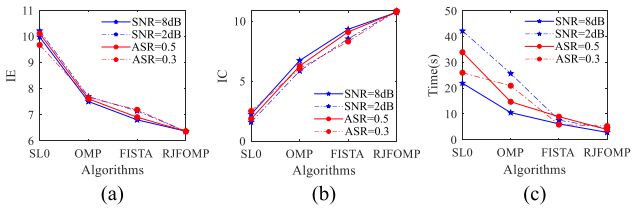

FIGURE 12. IE, IC and time of imaging results in Figs. 10 and 11. (a) IE; (b) IC; (c) Time.

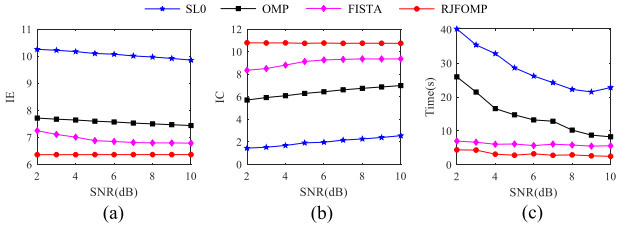

FIGURE 13. Monte-Carlo experimental results of SNR for data2. (a) IE; (b) IC; (c) Time.

Firstly, take the simulated data1 with CM motion error mode as an example. Under the condition of ASR = 0.5, the

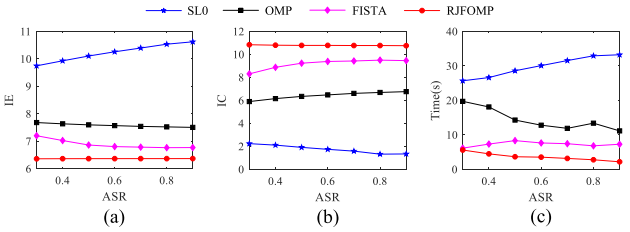

FIGURE 14. Monte-Carlo experimental results of ASR for data2. (a) IE; (b) IC; (c) Time.

imaging results of four algorithms at SNR = 8dB and 2dB are shown in Fig. 5. Under the condition of SNR = 5dB, the imaging results of four algorithms at ASR = 0.5 and 0.3 are shown in Fig. 6. The IE, IC and Time of imaging results in Figs. 5 and 6 are calculated in Fig. 7. As is seen from Figs. 5 and 6, SL0 and OMP algorithms have poor ability of noise suppression. The imaging quality of FISTA decreases under low SNR and ASR. Instead, RJFOMP has the best imaging quality under all given conditions. The numerical results in Fig. 7 also confirm the best imaging quality and the fastest imaging speed of RJFOMP.

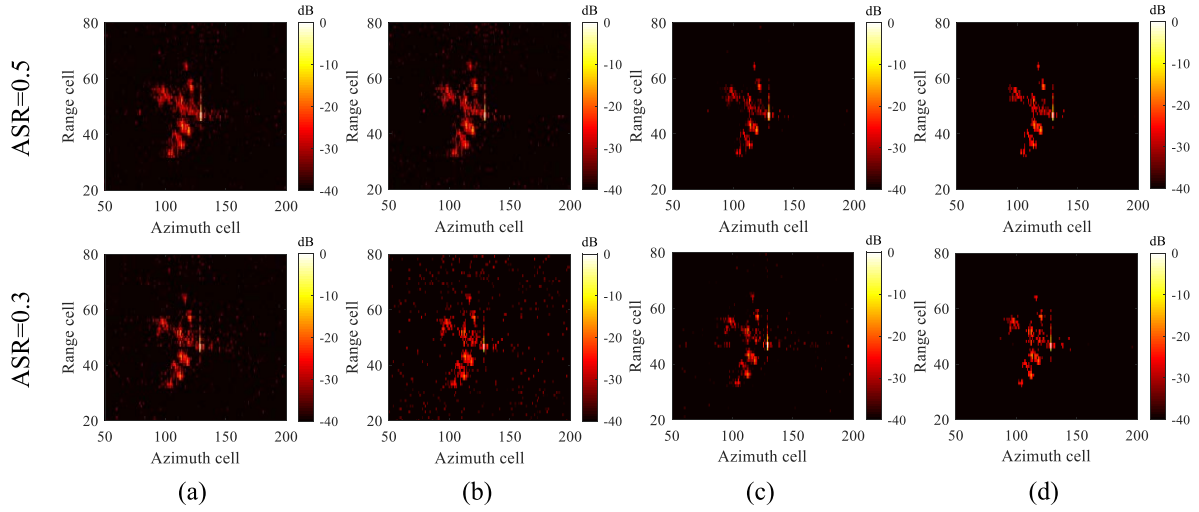

FIGURE 15. Imaging results of different algorithms under different ASRs for data3. (a) SL0; (b) OMP; (c) FISTA; (d) RJFOMP.

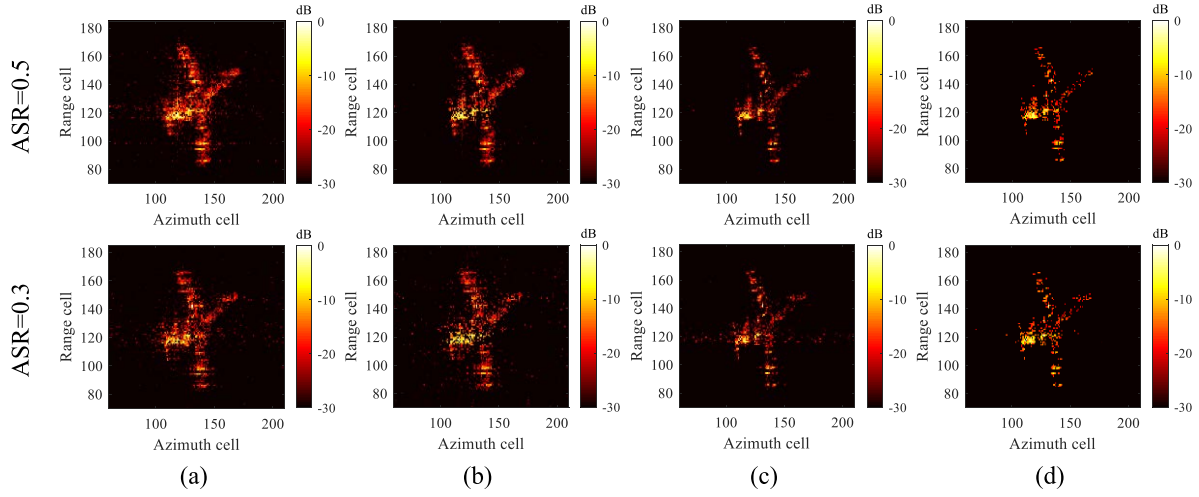

FIGURE 16. Imaging results of different algorithms under different ASRs for data4. (a) SL0; (b) OMP; (c) FISTA; (d) RJFOMP.

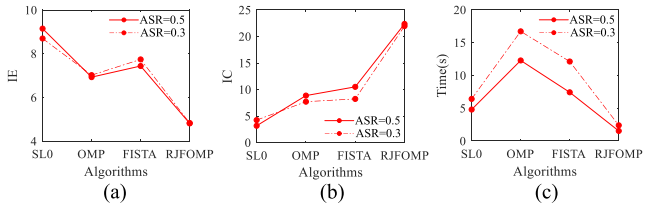

FIGURE 17. IE, IC and time of imaging results in Fig. 15. (a) IE; (b) IC; (c) Time.

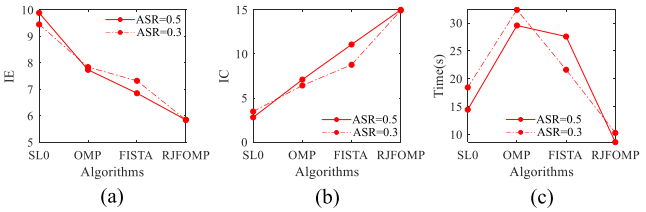

FIGURE 18. IE, IC and time of imaging results in Fig. 16. (a) IE; (b) IC; (c) Time.

For the purpose of increasing the reliability of performance verification, Monte-Carlo is used to further compare the imaging performance of different algorithms under different SNRs and ASRs. The SNR is set to range from 2dB to 10dB in steps of 1dB with the ASR being fixed as 0.5, and 100 trials are performed on each SNR. Similarly, the ASR is set to range from 0.3 to 0.9 in steps of 0.1 with the SNR being fixed as 5dB, and 100 trials are performed on each ASR. The average IE, IC and Time versus each SNR and ASR are presented in Figs. 8 and 9, respectively. It can be seen that RJFOMP has the smallest IE and Time, and the highest IC under different SNRs and ASRs, further verifying its robustness.

Then, take the simulated data2 with NCM motion error mode as an example, and set the same simulation conditions as data1. The imaging results of four algorithms under different SNRs and ASRs are shown in Figs. 10 and 11, respectively. The IE, IC and Time of imaging results of Figs. 10 and 11 are calculated in Fig. 12. It can be seen that although the motion error mode of data2 is different from

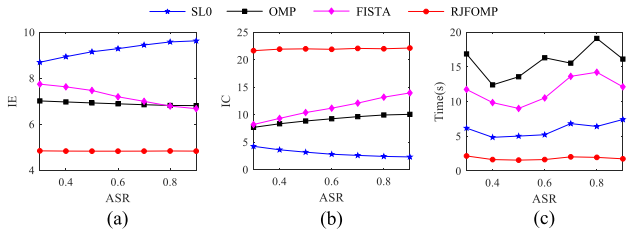

FIGURE 19. Monte-Carlo experimental results of ASR for data3. (a) IE; (b) IC; (c) Time.

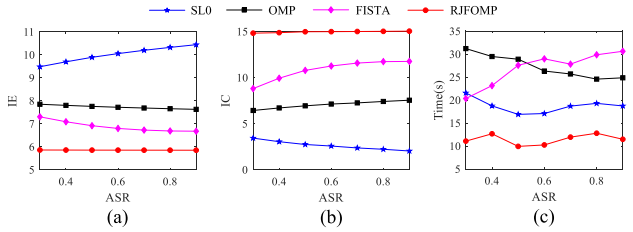

FIGURE 20. Monte-Carlo experimental results of ASR for data4. (a) IE; (b) IC; (c) Time.

data1, the imaging results of joint phase adjustment and ISAR imaging are similar after IGME range alignment. Compared with the other three algorithms, RJFOMP also has the best imaging quality and the highest imaging efficiency under all given conditions. In addition, the ranges of SNR and ASR in Monte-Carlo experiments are the same as data1. The average IE, IC and Time versus each SNR and ASR are presented in Figs. 13 and 14, respectively. It can be seen that RJFOMP has the smallest IE and Time, and the highest IC under different SNRs and ASRs as well.

Eventually, the effectiveness of the proposed algorithm is further illustrated by the measured data3 and data4, the motion error modes of which are CM and NCM, respectively. For data3, under the condition of SNR $=$ 0dB, the imaging results of four algorithms at ASR $=$ 0.5 and 0.3 are shown in Fig. 15. For data4, under the condition of SNR $=$ 10dB, the imaging results of four algorithms at ASR $=$ 0.5 and 0.3 are shown in Fig. 16. The IE, IC and Time of imaging results in Figs. 15 and 16 are calculated in Figs. 17 and 18, respectively. Similar to the previous simulated data, we further perform 100 Monte-Carlo trials on the measured data. For data3, the ASR is set to range from 0.3 to 0.9 in steps of 0.1 with the SNR being fixed as 0dB, and the ASR is set to range from 0.3 to 0.9 in steps of 0.1 with the SNR being fixed as 10dB for data4. The average IE, IC and Time versus each ASR for data3 and data 4 are presented in Figs. 19 and 20, respectively. In Figs. 15-20, compared with the other three algorithms, the imaging quality of RJFOMP under different ASRs for data3 and data4 is improved, and the imaging time is relatively short, indicating the applicability of the proposed algorithm to the measured data.

V. CONCLUSION

In this paper, based on the signal model of joint phase adjustment and ISAR imaging, a novel TMC method for ISAR imaging is proposed. In order to improve the accuracy of range alignment, an IGME range alignment method is presented by the interpolation processing. Then, RJFOMP algorithm is applied to ISAR imaging, MEM is used to estimate the phase error, and the joint optimization of phase adjustment and ISAR imaging is realized through the cyclic iteration. The experimental results of both simulated and measured data indicate that IGME has good accuracy of range alignment, and the joint processing of phase adjustment and ISAR imaging can improve the accuracy of phase adjustment. In addition, RJFOMP has excellent imaging performance under different SNRs and ASRs when used in the joint processing. However, the proposed method also has certain limitations. For example, IGME improves the accuracy of range alignment at the cost of time. The imaging performance of largely gapped data needs to be improved. The imaging time of the joint processing is relatively long, which has great advantages in imaging scenes with low time requirements. Therefore, the next research focuses on the improvement of algorithm performance and ISAR imaging under the condition of complex motion.

REFERENCES

[1] X. Wei, J. Yang, M. Lv, W. Chen, X. Ma, M. Long, and S. Xia, "ISAR high-resolution imaging method with joint FISTA and VGGNet," *IEEE Access*, vol. 9, pp. 86685–86697, 2021.
[2] L. Zhang, J.-L. Sheng, J. Duan, M.-D. Xing, Z.-J. Qiao, and Z. Bao, "Translational motion compensation for ISAR imaging under low SNR by minimum entropy," *EURASIP J. Adv. Signal Process.*, vol. 33, no. 1, pp. 1–19, Dec. 2013.
[3] S. Shao, L. Zhang, and H. Liu, "High-resolution ISAR imaging and motion compensation with 2-D joint sparse reconstruction," *IEEE Trans. Geosci. Remote Sens.*, vol. 58, no. 10, pp. 6791–6811, Oct. 2020.
[4] I. J. Gupta, M. J. Beals, and A. Moghaddar, "Data extrapolation for high resolution radar imaging," *IEEE Trans. Antennas Propag.*, vol. 42, no. 11, pp. 1540–1545, Nov. 1994.
[5] Y. Wang and Q. Liu, "Super-resolution sparse aperture ISAR imaging of maneuvering target via the RELAX algorithm," *IEEE Sensors J.*, vol. 18, no. 21, pp. 8726–8738, Nov. 2018.
[6] R. Bose, A. Freedman, and B. D. Steinberg, "Sequence CLEAN: A modified deconvolution technique for microwave images of contiguous targets," *IEEE Trans. Aerosp. Electron. Syst.*, vol. 38, no. 1, pp. 89–97, Jan. 2002.
[7] S. Shao, L. Zhang, J. Wei, and H. Liu, "Two-dimension joint super-resolution ISAR imaging with joint motion compensation and azimuth scaling," *IEEE Geosci. Remote Sens. Lett.*, vol. 18, no. 8, pp. 1411–1415, Aug. 2021.
[8] D. L. Donoho, "Compressed sensing," *IEEE Trans. Inf. Theory*, vol. 52, no. 4, pp. 1289–1306, Apr. 2006.
[9] J. A. Tropp and A. C. Gilbert, "Signal recovery from random measurements via orthogonal matching pursuit," *IEEE Trans. Inf. Theory*, vol. 53, no. 12, pp. 4655–4666, Dec. 2007.
[10] A. Beck and M. Teboulle, "A fast iterative shrinkage-thresholding algorithm for linear inverse problems," *SIAM J. Imag. Sci.*, vol. 2, no. 1, pp. 183–202, Mar. 2009.
[11] W. Chen, L. Xiang, J. Yang, X. Ma, and N. Ma, "Inverse synthetic aperture radar imaging with two-dimensional cluster sparse structure by matrix-formed iteratively reweighted complex approximate message passing," *J. Appl. Remote Sens.*, vol. 12, no. 3, Aug. 2018, Art. no. 035013.
[12] H. R. Hashempour, "Sparsity-driven ISAR imaging based on two-dimensional ADMM," *IEEE Sensors J.*, vol. 20, no. 22, pp. 13349–13356, Nov. 2020.
[13] S. Zhang, Y. Liu, and X. Li, "Micro-Doppler effects removed sparse aperture ISAR imaging via low-rank and double sparsity constrained ADMM and linearized ADMM," *IEEE Trans. Image Process.*, vol. 30, pp. 4678–4690, 2021.
[14] S. Zhang, Y. Liu, and X. Li, "Fast sparse aperture ISAR autofocusing and imaging via ADMM based sparse Bayesian learning," *IEEE Trans. Image Process.*, vol. 29, pp. 3213–3226, 2020.

[15] R. Li, S. Zhang, C. Zhang, Y. Liu, and X. Li, "Deep learning approach for sparse aperture ISAR imaging and autofocusing based on complex-valued ADMM-Net," *IEEE Sensors J.*, vol. 21, no. 3, pp. 3437–3451, Feb. 2021.
[16] M. Dakovic, L. Stankovic, and S. Stankovic, "Gradient algorithm based ISAR image reconstruction from the incomplete dataset," in *Proc. 3rd Int. Workshop Compressed Sens. Theory Appl. Radar, Sonar Remote Sens. (CoSeRa)*, Jun. 2015, pp. 6–10.
[17] S. Zhang, Y. Liu, and X. Li, "Minimum entropy based ISAR motion compensation with low SNR," in *Proc. IEEE China Summit Int. Conf. Signal Inf. Process.*, Jul. 2013, pp. 593–596.
[18] J. Wei, S. Shao, H. Ma, P. Wang, L. Zhang, and H. Liu, "High-resolution ISAR imaging with modified joint range spatial-variant autofocus and azimuth scaling," *Sensors*, vol. 20, no. 18, p. 5047, Sep. 2020.
[19] D. Zhu, L. Wang, Y. Yu, Q. Tao, and Z. Zhu, "Robust ISAR range alignment via minimizing the entropy of the average range profile," *IEEE Geosci. Remote Sens. Lett.*, vol. 6, no. 2, pp. 204–208, Apr. 2009.
[20] Y. Li, T. Zhang, Z. Ding, W. Gao, and J. Chen, "An improved inverse synthetic aperture radar range alignment method based on maximum contrast," *J. Eng.*, vol. 2019, no. 19, pp. 5467–5470, Oct. 2019.
[21] Y. Xiang, Z. Dai-Yin, Z. Jing-Dong, and J. Rui, "Motion compensation algorithm based on the designing structured Gram matrices method," *IET Radar, Sonar Navigat.*, vol. 8, no. 3, pp. 209–219, Mar. 2014.
[22] Z. Zhu, X. Qiu, and Z. She, "ISAR motion compensation using modified Doppler centroid tracking method," *Acta Electronica Sinica*, vol. 25, no. 3, pp. 65–69, Mar. 1997.
[23] D. Zhu, X. Yu, and Z. Zhu, "Algorithms for compressed ISAR autofocusing," in *Proc. IEEE CIE Int. Conf. Radar*, Oct. 2011, pp. 533–536.
[24] J. Wang, X. Liu, and Z. Zhou, "Minimum-entropy phase adjustment for ISAR," *IEE Proc.-Radar, Sonar Navigat.*, vol. 151, no. 4, pp. 203–209, Aug. 2004.
[25] J. Cai, M. Martorella, S. Chang, Q. Liu, Z. Ding, and T. Long, "Efficient nonparametric ISAR autofocus algorithm based on contrast maximization and Newton's method," *IEEE Sensors J.*, vol. 21, no. 4, pp. 4474–4487, Feb. 2021.
[26] N. Ö. Onhon and M. Cetin, "A sparsity-driven approach for joint SAR imaging and phase error correction," *IEEE Trans. Image Process.*, vol. 21, no. 4, pp. 2075–2088, Apr. 2012.
[27] Q. Hou, L. Fan, S. Su, and Z. P. Chen, "Compensation of phase errors for compressed sensing based ISAR imagery using inadequate pulses," *Prog. Electromagn. Res. M*, vol. 41, pp. 125–138, 2015.
[28] L. Wang, T. Huang, and Y. Liu, "Phase compensation and image autofocusing for randomized stepped frequency ISAR," *IEEE Sensors J.*, vol. 19, no. 10, pp. 3784–3796, May 2019.
[29] S. Zhang, Y. Liu, and X. Li, "Autofocusing for sparse aperture ISAR imaging based on joint constraint of sparsity and minimum entropy," *IEEE J. Sel. Topics Appl. Earth Observ. Remote Sens.*, vol. 10, no. 3, pp. 998–1011, Mar. 2017.
[30] S. Zhang, Y. Liu, and X. Li, "Computationally efficient sparse aperture isar autofocusing and imaging based on fast ADMM," *IEEE Trans. Geosci. Remote Sens.*, vol. 58, no. 12, pp. 8751–8765, Dec. 2020.
[31] M. Xing, R. Wu, J. Lan, and Z. Bao, "Migration through resolution cell compensation in ISAR imaging," *IEEE Geosci. Remote Sens. Lett.*, vol. 1, no. 2, pp. 141–144, Apr. 2004.
[32] L. Zhang, M. Xing, C. Qiu, J. Li, J. Sheng, Y. Li, and Z. Bao, "Resolution enhancement for inversed synthetic aperture radar imaging under low SNR via improved compressive sensing," *IEEE Trans. Geosci. Remote Sens.*, vol. 48, no. 10, pp. 3824–3838, Oct. 2010.
[33] Y. Fang, J. Wu, and B. Huang, "2D sparse signal recovery via 2D orthogonal matching pursuit," *Sci. China Inf. Sci.*, vol. 55, no. 4, pp. 889–897, Apr. 2012.
[34] H. R. Hashempour and A. Sheikhi, "Dynamic ISAR imaging and autofocusing of maneuvering targets based on sequential GP-SOONE method and eigenvalue decomposition," *IEEE Sensors J.*, vol. 19, no. 11, pp. 4045–4053, Jun. 2019.
[35] C. Yang, W. Feng, H. Feng, T. Yang, and B. Hu, "A sparsity adaptive subspace pursuit algorithm for compressive sampling," *Acta Electronica Sinica*, vol. 38, no. 8, pp. 1914–1917, Aug. 2010.
[36] J. Wang, S. Kwon, and B. Shim, "Generalized orthogonal matching pursuit," *IEEE Trans. Signal Process.*, vol. 60, no. 12, pp. 6202–6216, Dec. 2012.
[37] F. Zhu, Q. Zhang, J. B. Yan, F. F. Gu, and S. Liu, "Compressed sensing in ISAR imaging with sparse sub-aperture," in *Proc. IEEE CIE Int. Conf. Radar*, Oct. 2011, pp. 1463–1466.
[38] C. Zeng, W. Zhu, X. Jia, and L. Yang, "Sparse aperture ISAR imaging method based on joint constraints of sparsity and low rank," *IEEE Trans. Geosci. Remote Sens.*, vol. 59, no. 1, pp. 168–181, Jan. 2021.

XU WEI received the B.S. and M.S. degrees from the Air Force Early Warning Academy, Wuhan, China, in 2016 and 2018, respectively, where he is currently pursuing the Ph.D. degree. His research interests include compressive sensing and ISAR imaging.

JUN YANG received the Ph.D. degree from Air Force Engineering University, Xi'an, China, in 2003. He is currently a Professor with the Air Force Early Warning Academy, Wuhan, China. His research interests include radar systems, radar imaging, compressive sensing, and radar signal processing.

MINGJIU LV received the M.S. and Ph.D. degrees from the Air Force Early Warning Academy, Wuhan, China, in 2010 and 2018, respectively. He is currently a Lecturer with the Air Force Early Warning Academy. His research interests include compressive sensing and ISAR imaging.

WENFENG CHEN received the M.S. and Ph.D. degrees from the Air Force Early Warning Academy, Wuhan, China, in 2014 and 2018, respectively. He is currently a Lecturer with the Air Force Early Warning Academy. His research interests include compressive sensing and Bi-ISAR imaging.

XIAOYAN MA received the B.S. degree from the Nanjing University of Science and Technology, Nanjing, China, in 1982, the M.S. degree from the National University of Defense Technology, Changsha, China, in 1988, and the Ph.D. degree from Tsinghua University, Beijing, China, in 2002. He is currently a Professor with the Air Force Early Warning Academy, Wuhan, China. His main research interests include radar systems, target detection and imaging, as well as ISAR signal processing.